Spin Caloritronics Group, Research Center for Magnetic and Spintronic Materials, National Institute for Materials Science, Tsukuba 305-0047, Japan.

Multifunctional composite magnet realizing record-high transverse thermoelectric generation

We have created a novel functional material named "multifunctional composite magnet (MCM)", which simultaneously exhibits record-high transverse thermoelectric performance and permanent magnet features. Owing to the optimized composite structure and extremely low interfacial electrical and thermal resistivities, the power generation performance of our MCM-based thermopile module is not only record-high among transverse thermoelectric modules but also comparable to that of commercial modules utilizing the Seebeck effect. This multifunctionality will extend application fields of thermoelectrics to everywhere permanent magnets are used.

Image reproduced by permission of Ken-ichi Uchida from *Energy Environ. Sci.*, 2025, **18**, 4068

ROYAL SOCIETY
OF **CHEMISTRY**

rsc.li/ees

PAPER

Check for updates

Multifunctional composite magnet realizing record-high transverse thermoelectric generation†

Fuyuki Ando, [iD] *[a] Takamasa Hirai, [iD] [a] Abdulkareem Alasli, [iD] [b] Hossein Sepehri-Amin,[a] Yutaka Iwasaki,[a] Hosei Nagano[b] and Ken-ichi Uchida [iD] *[ac]

Permanent magnets are used in various products and essential for human society. If omnipresent permanent magnets could directly convert heat into electricity, they would lead to innovative energy harvesting and thermal management technologies. However, achieving such "multifunctionality" has been difficult due to poor thermoelectric performance of conventional magnets. In this work, we develop a multifunctional composite magnet (MCM) that enables giant transverse thermoelectric conversion while possessing permanent magnet features. MCM comprising alternately and obliquely stacked $SmCo_5/Bi_{0.2}Sb_{1.8}Te_3$ multilayers exhibits an excellent transverse thermoelectric figure of merit $z_{xy}T$ of 0.20 at room temperature owing to the optimized anisotropic structure and extremely low interfacial electrical and thermal resistivities between the $SmCo_5$ and $Bi_{0.2}Sb_{1.8}Te_3$ layers. The MCM-based thermopile module generates a maximum of 204 mW at a temperature difference of 152 K, whose power density normalized by the heat transfer area and temperature gradient is not only record-high among transverse thermoelectric modules but also comparable to those of commercial thermoelectric modules utilizing the Seebeck effect. The multifunctionality of our MCM provides unprecedented opportunities for energy harvesting and thermal management everywhere permanent magnets are currently used.

Broader context

For the realization of a carbon-neutral society, new core technologies for energy harvesting and thermal management are strongly desired in various factories and industries including automobile and electronics. We have created a novel functional material named "multifunctional composite magnet (MCM)", which simultaneously exhibits practically applicable giant transverse thermoelectric conversion and permanent magnet features. Our developed MCM comprising alternately and obliquely stacked $SmCo_5/Bi_{0.2}Sb_{1.8}Te_3$ multilayers exhibits an excellent transverse thermoelectric figure of merit of 0.20 at room temperature owing to the optimized anisotropic structure and extremely low interfacial electrical and thermal resistivities between the $SmCo_5$ and $Bi_{0.2}Sb_{1.8}Te_3$ layers. The power generation performance of our MCM-based thermopile module is not only record-high among transverse thermoelectric modules but also comparable to that of commercial modules utilizing the Seebeck effect. This multifunctionality will extend application fields of thermoelectrics to everywhere permanent magnets are used.

1. Introduction

Transverse thermoelectric effects realize the interconversion between the charge and heat currents in the orthogonal direction. The orthogonal geometry simplifies the thermoelectric device architecture because it can eliminate substrates, electrodes, and their junctions in the thermal circuit. This junction-less structure makes it possible to apply a larger temperature gradient ∇T to thermoelectric materials owing to the absence of substrates, improve the thermoelectric conversion efficiency owing to the lack of interfacial thermal resistance between the thermoelectric materials and electrodes, and suppress thermal deterioration at hot-side junctions, all of which are significant issues for conventional longitudinal thermoelectric modules based on the Seebeck effect.[1–3] To utilize these geometrical advantages, many recent studies have focused on the development of physics, materials science, and device architectures for transverse thermoelectric conversion.

[a] *National Institute for Materials Science, Tsukuba 305-0047, Japan. E-mail: ANDO.Fuyuki@nims.go.jp, UCHIDA.Kenichi@nims.go.jp*

[b] *Department of Mechanical Systems Engineering, Nagoya University, Nagoya 464-8603, Japan*

[c] *Department of Advanced Materials Science, Graduate School of Frontier Sciences, The University of Tokyo, Kashiwa 277-8561, Japan*

† Electronic supplementary information (ESI) available. See DOI: https://doi.org/10.1039/d4ee04845h

4068 | *Energy Environ. Sci.*, 2025, **18**, 4068–4079

This journal is © The Royal Society of Chemistry 2025

Paper

The transverse thermoelectric effects are classified into various mechanisms.[4] Following the classification in ref. 4, the four mechanisms are related to magnetism or spin: the ordinary and anomalous Nernst effects,[5–21] the spin Seebeck effect,[22] and the Seebeck-effect-driven anomalous Hall effect.[23] The other mechanisms are unrelated to magnetism or spin: the off-diagonal Seebeck effects (ODSEs)[3,24–40] in natural anisotropic crystals and artificial anisotropic composites. The ordinary Nernst effect has been studied for a long period[5] to enable large transverse thermoelectric conversion, but its operation requires the application of a large external magnetic field (typically above 2 T). Recently, with the development of topological materials science and spin caloritronics, the anomalous Nernst effect (ANE) in magnetic materials has been intensively studied.[7–10,12–14,17,19] Thermoelectric conversion through ANE requires spatially uniform magnetization, which is typically achieved by applying external magnetic fields. From an application point of view, ANE for permanent magnets with remanent magnetization M_r has been studied to achieve magnetic-field-free operation of transverse thermoelectric conversion.[11,15,20] Although these developments realize multifunctionality enabling transverse thermoelectric conversion, the tiny transverse thermoelectric figure of merit $z_{xy}T$ for ANE ($<10^{-3}$) hinders future applications of multifunctional magnets. By contrast, the studies on ODSEs have independently progressed and predicted a considerably higher $z_{xy}T$ (> 0.1 at room temperature) compared with that for ANE.[28,33,34,37–39] ODSE in an artificial composite system is enhanced when two materials having opposite Seebeck coefficients, i.e., p- and n-type materials, and large differences in electrical and thermal conductivities are alternately and obliquely stacked (artificially tilted multilayers, ATMLs).[27] However, despite the wide material selectivity, no attempts have been made to integrate the magnetic functionality into ATMLs, except for a recent study.[40] Although ATMLs consisting of $Nd_2Fe_{14}B$-type permanent magnets and $Bi_{88}Sb_{12}$ have been developed, their transverse thermoelectric performance is poor ($z_{xy}T < 2.0 \times 10^{-3}$) because the sign of the Seebeck coefficient of $Nd_2Fe_{14}B$ is the same as that of $Bi_{88}Sb_{12}$.

Here, we have developed MCM that exhibits giant transverse thermoelectric conversion in addition to large remanent magnetization and coercivity (Fig. 1). Our MCM, comprising alternately and obliquely stacked $SmCo_5$-type permanent magnets ($SmCo_5$) and thermoelectric $Bi_{0.2}Sb_{1.8}Te_3$ (BST) slabs, experimentally exhibits an excellent $z_{xy}T$ of 0.20 at room temperature owing to the optimized anisotropic composite structure and extremely low interfacial electrical and thermal resistivities between the $SmCo_5$ and BST layers. Utilizing these high-performance MCM elements, we constructed a lateral thermopile module to obtain a higher thermoelectric voltage while maintaining the magnetic functionality. The MCM-based module exhibits an output power P of 204 mW at a temperature difference ΔT of 152 K, which corresponds to the record-high normalized power density per heat transfer area and ∇T^2 of 0.17 mW cm^{-2} (K mm^{-1})$^{-2}$ among those of the transverse thermoelectric modules.
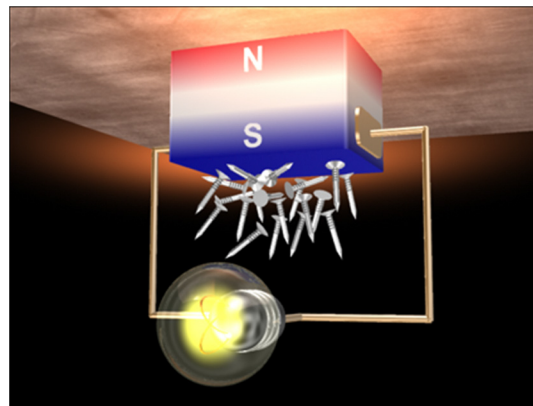

Fig. 1 Schematic of the concept of MCM exhibiting strong magnetic force and superior transverse thermoelectric performance simultaneously.

2. Results and discussion

2.1 Magnetic and analytical transverse thermoelectric properties

ODSE in ATMLs generates an electric field **E** in the direction perpendicular to ∇T owing to the anisotropic transport properties in the tilted axes with respect to the ∇T direction (Fig. 2a). When the thermal conductivity of the two constituent materials is different, the heat current $\mathbf{J}_q$ nonuniformly flows in ATMLs by the application of ∇T because $\mathbf{J}_q$ is likely to flow in a path with a high thermal conductivity, that is, in the direction parallel to high-thermal-conductive layers and perpendicular to low-thermal-conductive layers. Then, through the thermoelectric conversion by the Seebeck effect in the p- and n-type layers, the transverse component of the charge current $\mathbf{J}_c$ (or **E**) is additively generated (see Note S1 and Fig. S1, ESI,† where the nonuniform charge-to-heat current conversion due to the origin of ODSE was confirmed by the lock-in thermography method). Here, the primary characteristic of ODSE is that, even if the Seebeck coefficient S of the constituent material is not high, $z_{xy}T$ can be enhanced by combining p- and n-type materials whose electrical resistivity ρ and thermal conductivity κ are largely different. Indeed, ATMLs composed of metals and thermoelectric semiconductors, such as n-type Ni/p-type $Bi_{0.5}Sb_{1.5}Te_3$,[28,30,31,34] n-type $YbAl_3$/p-type $Bi_{0.5}Sb_{1.5}Te_3$,[33] p-type Fe/n-type $Bi_2Te_{2.7}Se_{0.3}$,[37] and n-type Co/p-type $Bi_{0.5}Sb_{1.5}Te_3$,[38] have been predicted to exhibit $z_{xy}T > 0.1$ at room temperature as well as n-type $Bi_2Te_{2.7}Se_{0.3}$/p-type $Bi_{2-x}Sb_xTe_3$.[39] $SmCo_5$, which is a widely known permanent magnet for its strong magnetic force and excellent thermal stability,[41] also has metallic transport properties and negative S.[11,15] Thus, we selected p-type BST as a counterpart material for $SmCo_5$, as ρ and κ are one order smaller than those of $SmCo_5$ and the sign of S is opposite (Fig. S2, ESI†).

We predict the superior transverse thermoelectric performance in $SmCo_5$/BST-based ATML using analytical matrix calculations. Based on Goldsmid's method,[27] the thermoelectric parameters, i.e., electrical resistivity ρ_{ij}, thermal conductivity κ_{ij}, and thermopower S_{ij} can be calculated neglecting
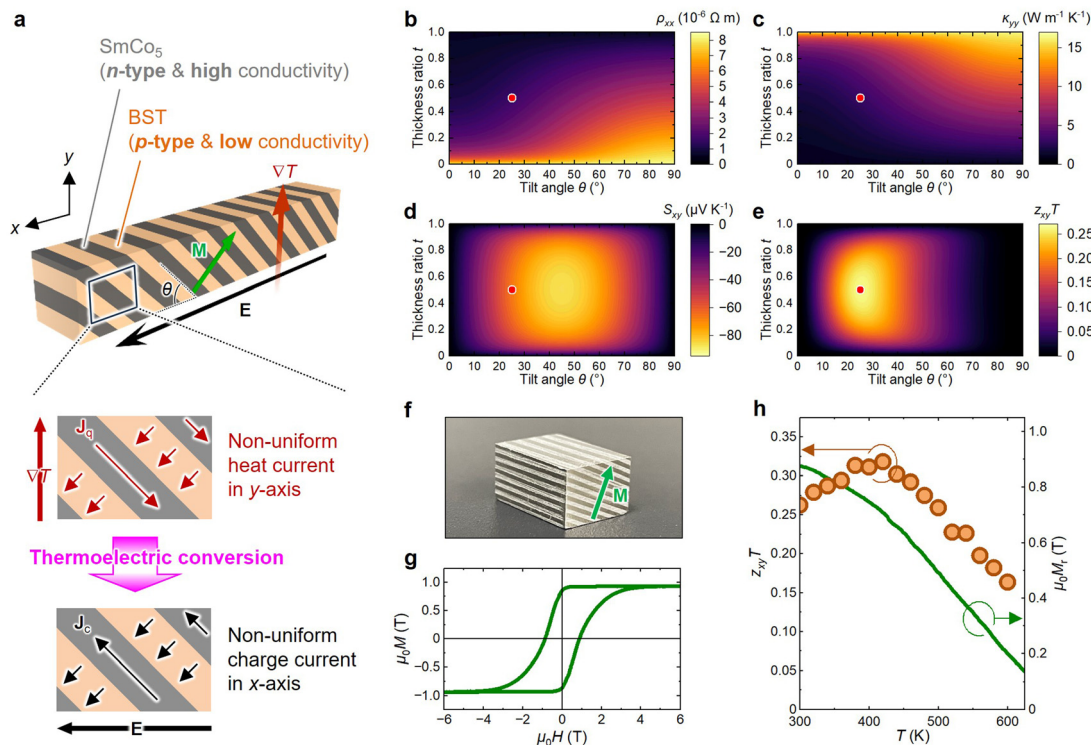
Fig. 2 Magnetic and analytical transverse thermoelectric properties of MCM. (a) Schematic of MCM composed of SmCo$_5$ and BST with a tilt angle θ. An ATML structure induces a nonuniform heat current $\mathbf{J}_q$ by the application of a temperature gradient ∇T in the y-axis, which generates a charge current $\mathbf{J}_c$ (or an electric field $\mathbf{E}$) in the transverse direction through thermoelectric conversion by the Seebeck effect. Remanent magnetization in the SmCo$_5$ layers M_r is oriented along the stacking direction. (b)–(e) Contour plots of the analytical electrical resistivity in the x-axis ρ_{xx} (b), thermal conductivity in the y-axis κ_{yy} (c), off-diagonal Seebeck coefficient S_{xy} (d), and transverse thermoelectric figure of merit $z_{xy}T$ (e) as a function of the thickness ratio of the SmCo$_5$ layer t and θ in SmCo$_5$/BST-based MCM at 300 K. Red points indicate the optimum t and θ to maximize $z_{xy}T$, i.e., $t = 0.5$ and $\theta = 25°$. (f) Photograph of SmCo$_5$/BST-based MCM. (g) Magnetization M of the SmCo$_5$ slab as a function of an external magnetic field H in its magnetic easy axis direction. μ_0 is the vacuum permeability. (h) Temperature T dependences of the calculated $z_{xy}T$ at $t = 0.5$ and $\theta = 25°$ and M_r of the SmCo$_5$ slab.

interfacial contributions. As depicted in Fig. 2a, the off-diagonal Seebeck coefficient S_{xy} is defined by generated $\mathbf{E}$ in the x-direction and applied ∇T in the y-direction. ρ (κ) is a proportionality factor between $\mathbf{E}$ ($\mathbf{J}_q$) and $\mathbf{J}_c$ (∇T). Thus, κ_{yy} and ρ_{xx} are used for $z_{xy}T$ because the applied ∇T and generated $\mathbf{E}$ are in y- and x-directions for the transverse thermoelectric conversion. The thermoelectric parameters of the SmCo$_5$/BST multilayers in the direction parallel ($\rho_\parallel$, $\kappa_\parallel$, and $S_\parallel$) and perpendicular ($\rho_\perp$, $\kappa_\perp$, and $S_\perp$) to the stacking plane are analytically calculated using the electrical resistivities ρ_{SmCo} and ρ_{BST}, thermal conductivities κ_{SmCo} and κ_{BST}, and Seebeck coefficients S_{SmCo} and S_{BST} for SmCo$_5$ and BST, respectively:[27]

$$\rho_\parallel = \frac{\rho_{SmCo}\rho_{BST}}{(1-t)\rho_{SmCo} + t\rho_{BST}}$$

$$\rho_\perp = t\rho_{SmCo} + (1-t)\rho_{BST} \tag{1}$$

$$\kappa_\parallel = t\kappa_{SmCo} + (1-t)\kappa_{BST}$$

$$\kappa_\perp = \frac{\kappa_{SmCo}\kappa_{BST}}{(1-t)\kappa_{SmCo} + t\kappa_{BST}} \tag{2}$$

$$S_\parallel = \frac{t\rho_{BST}S_{SmCo} + (1-t)\rho_{SmCo}S_{BST}}{t\rho_{BST} + (1-t)\rho_{SmCo}}$$

$$S_\perp = \frac{t\kappa_{BST}S_{SmCo} + (1-t)\kappa_{SmCo}S_{BST}}{t\kappa_{BST} + (1-t)\kappa_{SmCo}} \tag{3}$$

where $t = d_{SmCo}/(d_{SmCo} + d_{BST})$ denotes the thickness ratio of the SmCo$_5$ layer and d_{SmCo} (d_{BST}) the thickness of the SmCo$_5$ (BST) layer. When the homogeneous SmCo$_5$/BST multilayers are rotated in the xy-plane with the tilt angle θ (Fig. 2a), the transverse thermoelectric properties by ODSE can be expressed as

$$\rho_{xx} = \rho_\parallel \cos^2\theta + \rho_\perp \sin^2\theta \tag{4}$$

$$\kappa_{yy} = \kappa_\parallel \sin^2\theta + \kappa_\perp \cos^2\theta \tag{5}$$

$$S_{xy} = (S_\parallel - S_\perp)\sin\theta\cos\theta \tag{6}$$

Then, the transverse thermoelectric figure of merit $z_{xy}T$ is given by

$$z_{xy}T = \frac{S_{xy}^2}{\rho_{xx}\kappa_{yy}}T \tag{7}$$

Fig. 2b–e show the thickness ratio t and tilt angle θ dependences of the transverse thermoelectric properties for SmCo$_5$/BST-based ATML, obtained by substituting the measured properties of SmCo$_5$ and BST into eqn (1)–(7) (see also Note S2 and Fig. S3, ESI,† where the calculated ρ_{ij}, κ_{ij}, and S_{ij} were shown). We find that the calculated $z_{xy}T$ in SmCo$_5$/BST-based ATML reaches 0.26 at the optimum t of 0.5 and θ of 25° at T = 300 K (see red points in Fig. 2b–e). Furthermore, we calculated the temperature T dependence of ρ_{xx}, κ_{yy}, S_{xy}, and $z_{xy}T$ in the range of 300–600 K at t = 0.5 and θ = 25° (Fig. 2h and Fig. S4, ESI†). The $z_{xy}T$ value reaches a maximum of 0.32 at 420 K, which is more than two orders of magnitude higher than that of Nd$_2$Fe$_{14}$B/BiSb-based ATML.[40]

To experimentally demonstrate the expected performance as MCM, we synthesized SmCo$_5$/BST-based ATML using the calculated optimum θ and t values. SmCo$_5$ circular disks and BST powders were alternately stacked and bonded using spark plasma sintering (SPS), followed by cutting the sintered multilayer into tilted rectangular blocks (see Fig. 2f and the Experimental section for details). The accuracies of t and θ in the ATML block were estimated to be 0.50 ± 0.05 and 25 ± 1°, respectively. The elemental distribution maps of Sm, Co, Bi, Sb, and Te were obtained using scanning electron microscopy with energy dispersive X-ray spectroscopy (SEM-EDX). The low magnification EDX mapping of Sb, Te, and Co and the atomic ratio profile indicate no complex elemental migrations between the

SmCo$_5$ and BST layers (Fig. S5, ESI†). Then, from the high magnification image around the SmCo$_5$/BST interface shown in Fig. 3a, we recognize the growth of interfacial diffusion layers with a thickness of approximately 10 μm without interfacial voids. The atomic ratio profile in the stacking direction of the SmCo$_5$ and BST multilayers (Fig. 3b) reveals that the interfacial diffusion layers of CoTe$_a$-based compounds (1.5 < a < 2.0) are formed, which act as adhesive bonds. The magnetic easy axis of the SmCo$_5$ disks was out-of-plane. Fig. 2g shows the magnetization M of the SmCo$_5$ portion cut from the ATML as a function of the magnetic field H perpendicular to the stacking plane. The SmCo$_5$ layers exhibit a large M_r of 0.86 T and a coercivity of 0.87 T without deterioration even after sinter-bonding with the BST layers, which confirms that SmCo$_5$/BST-based ATML operates as MCM. Fig. 2h shows the T dependence of M_r, where the permanent magnet nature is sustained above 600 K owing to the excellent thermal stability of magnetism of SmCo$_5$.

2.2 Interfacial electrical and thermal resistivities

To verify the transverse thermoelectric performance of SmCo$_5$/BST-based MCM, it is important to characterize the interfacial electrical and thermal transport properties at the SmCo$_5$/BST junctions because they cause a degradation from the calculated properties shown in Fig. 2h as well as the thermoelectric material/electrode junctions in longitudinal thermoelectric devices.[2,42–44] Despite their importance, the quantitative
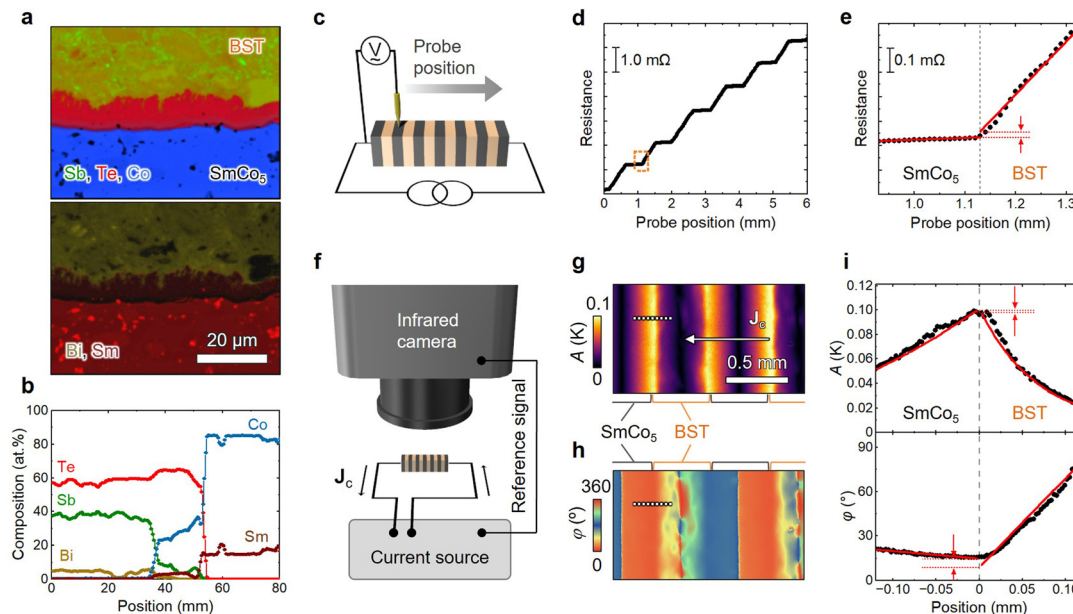

Fig. 3 Contribution of the interfacial transport properties to the transverse thermoelectric performance of MCM. (a) SEM-EDX images of the cross section of the SmCo$_5$/BST multilayer. (b) Line profile of the atomic ratios of Sm, Co, Bi, Sb, and Te across the stacking direction. (c) Schematic of the four-terminal resistance measurement setup to investigate the spatial distribution of the electrical resistance by sweeping the probe position. (d) Probe position dependence of the electrical resistance in the SmCo$_5$/BST multilayer in the stacking direction and (e) its enlarged view indicated by an orange dotted square in (d). Gray dotted line is the approximate position of the SmCo$_5$/BST interface, where a gap indicated by red arrows corresponds to the interfacial electctical resistance. (f) Schematic of the LIT measurement while applying the square-wave-modulated charge current **J**$_c$ with the amplitude J_c and frequency f. Lock-in amplitude A (g) and phase φ (h) images of the cross section of the SmCo$_5$/BST multilayer at J_c = 1 A and f = 25 Hz. (i) Line profiles of A and φ across the SmCo$_5$/BST interface for the white dotted lines with a length of 101 pixels in (g) and (h). Red curves represent the fitting functions using the one-dimensional heat equation.

investigation of the interfacial transport properties has not been attempted in previous studies.[30,33,34,37,38,40] In this study, we experimentally characterized the interfacial electrical and thermal resistivities and their contributions to the volumetric resistances.

First, we characterized the interfacial electrical resistance between the $SmCo_5$ and BST layers by measuring the spatial distribution of the electrical resistance. To distinguish the resistances originating from the bulk of $SmCo_5$, bulk of BST, and their interfaces, we prepared a rectangular sample comprising the $SmCo_5$/BST multilayer in which the cut angle was perpendicular to the stacking plane (*i.e.*, $\theta = 90°$). As shown in Fig. 3c, the four-terminal ac resistance was measured while the probe was scanned along the stacking direction. The measurement results shown in Fig. 3d revealed a step-like behavior reflecting the different electrical resistivities of $SmCo_5$ and BST layers, wherein the electrical resistivity of $SmCo_5$ is much smaller than that of BST (Fig. S2, ESI†). Significantly, when we focus on an interface between the $SmCo_5$ and BST layers (Fig. 3e), the position of which is indicated by a gray dotted line, the resistance profile was observed to be almost continuous. The interfacial electrical resistivity is estimated by linearly fitting the resistance profiles in the $SmCo_5$ and BST layers and extrapolating the fitting functions to the interface position (red arrows in Fig. 3e). Then, the averaged interfacial electrical resistivity at several interfaces is calculated to be 0.4 ± 1.2 μΩ cm². This unusually low interfacial resistivity, comparable to lowest-level contact resistivities for thermoelectric devices,[42] can be attributed to the metallic properties of $CoTe_a$-based diffusion layers,[45–47] whose resistivity is comparable to that of $SmCo_5$. Meanwhile, the volume resistance–area product of the 0.5-mm-thick $SmCo_5$ and BST layers was estimated to be 64 ± 2 μΩ cm⁻² from the slopes of the fitting functions. Thus, the ratio of the interfacial electrical resistance to the volumetric resistance was 1.2%, which is negligibly small within the margin of the experimental error.

The interfacial thermal resistance was also characterized using the lock-in thermography (LIT) measurements[48–51] for the same $SmCo_5$/BST multilayer sample with $\theta = 90°$. Fig. 3f shows a schematic of the LIT measurement setup. A square-wave-modulated $\mathbf{J}_c$ with an amplitude $\mathbf{J}_c$ of 1 A and a frequency f of 25 Hz, which guarantee the sensitivity of the interfacial thermal resistance in the order of 10^{-7} m² K W⁻¹,[49] was applied to the sample in a direction perpendicular to the stacking plane. The thermal images were continuously captured while applying $\mathbf{J}_c$ to observe the temperature modulation due to the Peltier-effect-induced heat current. When the heat current is discontinuous due to the difference in the Peltier coefficient at junctions, finite heat absorption and release appear in the vicinity of the interfaces.[50,51] By extracting the first harmonic response of the charge-current-induced temperature modulation through Fourier analysis and calculating the lock-in amplitude A and phase φ for each pixel of the thermal images, we visualized the pure contribution of the Peltier effect without contamination by Joule heating. Here, the A signals refer to the magnitude of the temperature change in linear response to $\mathbf{J}_c$

and φ signals to its sign and time delay due to the heat diffusion. A previous study[51] reported that the spatial profiles of the A and φ signals can be used to investigate the interfacial thermal resistance because a finite interfacial thermal resistance causes discontinuities in A and φ. We observed clear A signals near the $SmCo_5$/BST interfaces (Fig. 3g) and φ signals alternately changing from approximately 0° to 180° for each adjacent interface (Fig. 3h), which is consistent with the features of the Peltier-effect-induced temperature modulation. The line profiles of A and φ across the $SmCo_5$/BST interface are shown in Fig. 3i, where no obvious jumps appear at the interface position. By fitting the position dependence of A and φ using the one-dimensional heat equation,[51] the interfacial thermal resistance was estimated to be less than 1×10^{-6} m² K W⁻¹. Meanwhile, the thermal conductivities of $SmCo_5$ and BST layers were 16.3 and 1.0 W m⁻¹ K⁻¹ at 300 K, respectively (Fig. S2, ESI†). Thus, the contribution of the interfacial thermal resistance to the volumetric thermal resistance was also negligible (<0.4%).

2.3 Characterization of transverse thermoelectric performance

The above experiments ensure that the performance degradation due to the presence of multiple interfaces is quite small in our $SmCo_5$/BST-based MCM. To verify the small interfacial contribution to the transport behavior as depicted in Fig. 2a, we performed a two-dimensional finite element analysis of thermoelectric conversion in $SmCo_5$/BST-based MCM using the thermoelectric module of COMSOL Multiphysics software. A multilayer of $SmCo_5$ (0.5 mm) and BST (0.5 mm) with $\theta = 25°$ and dimensions of 12.4×8.3 mm was prepared as shown in Fig. 4a. The volumetric transport properties in Fig. S2 (ESI†) and interfacial electrical and thermal resistivities (0.4 μΩ cm² and 1×10^{-6} m² K W⁻¹) were used as the material parameters. The boundary condition was fixed so that the upper (lower) side was 303 (293) K to input ∇T in the y-direction and the left and right sides were thermally adiabatic. T and electric potential V distributions through the Seebeck effect were simultaneously calculated as shown in Fig. 4a and b. Then, we find a gradation of V in the direction perpendicular to the stacking plane, suggesting the generation of finite $\mathbf{E}$ in the x-direction through the Seebeck effect. By focusing on a central part of the multilayer and visualizing heat flux (Fig. 4a), we can see a heat-flux bending with respect to the input ∇T as depicted in Fig. 2a and T distribution inside the layers owing to the small interfacial thermal resistance. Thus, the generated $\mathbf{E}$ (Fig. 4b), localized in the BST layers due to the large $S_{BST}\nabla T$, also directs the oblique direction to the input ∇T, which is the origin of ODSE. Through this finite element analysis, we successfully reproduce the transverse thermoelectric conversion by ODSE[26,28] taking the interfacial resistances into account.

To experimentally determine $z_{xy}T$ with negligible contributions from the interfacial electrical and thermal resistances, we directly measured S_{xy} and ρ_{xx} in $SmCo_5$/BST-based MCM with the same dimension as that used in the finite element analysis at room temperature. Fig. 4c shows the measurement setup for
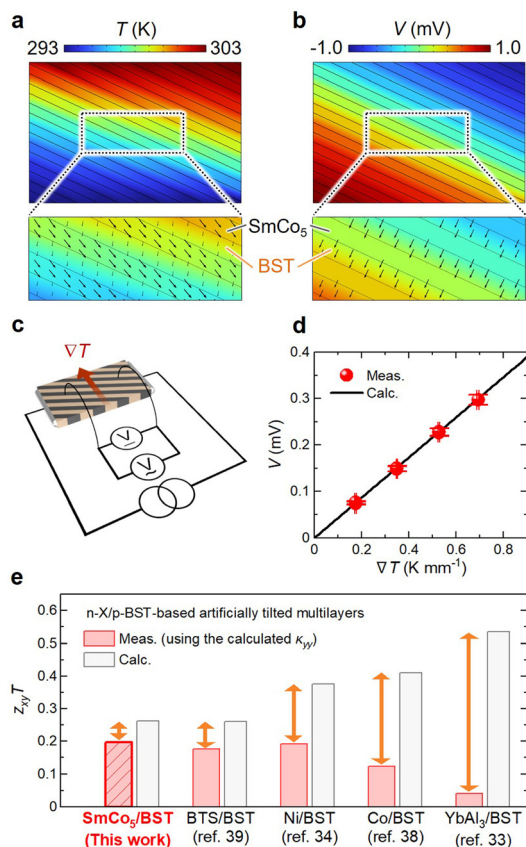
4072 | *Energy Environ. Sci.*, 2025, **18**, 4068–4079

This journal is © The Royal Society of Chemistry 2025

Fig. 4 (a) and (b) Finite-element analysis of (a) T and (b) electric potential V distributions through the Seebeck effect in SmCo$_5$/BST-based ATML taking the interfacial electrical and thermal resistances into account. Black arrows indicate a heat flux in (a) and **E** in (b). (c) Schematic of the setup for the direct measurement of S_{xy} and ρ_{xx}. (d) The temperature gradient ∇T dependence of the directly measured and analytically calculated thermoelectric voltage V values at room temperature. (e) Comparison of the measured and calculated $z_{xy}T$ at room temperature for various n-type X/p-type BST-based ATMLs (X = SmCo$_5$, Bi$_2$Te$_{2.7}$Se$_{0.3}$, Ni, Co, and YbAl$_3$). The calculated κ_{yy} values are used for both the measured and calculated $z_{xy}T$.

the transverse thermoelectric voltage V induced by a temperature gradient ∇T and the four-terminal ac resistance (see Experimental section for details). Fig. 4d shows that the V value linearly increases with ∇T and quantitatively agrees with the calculated line obtained from the analytically calculated S_{xy} (Fig. 2d), indicating that our MCM exhibits the ideally large transverse thermoelectric conversion. The S_{xy} value of SmCo$_5$/BST-based MCM was experimentally estimated to be 66.4 ± 1.1 μV K^{-1} at room temperature. The ac resistance was measured to be 1.54 ± 0.02 mΩ while the calculated one is 1.17 mΩ, where the increased resistance can be attributed to cracking in the SmCo$_5$ disks during the SPS process and to processing errors, such as θ and t.

Fig. 4e shows the comparison of $z_{xy}T$ between the values estimated from the analytical matrix calculation and direct measurement of S_{xy} and ρ_{xx} for various n-type X/p-type BST-based ATMLs, where X = SmCo$_5$, Bi$_2$Te$_{2.7}$Se$_{0.3}$ (BTS), Ni, Co, and YbAl$_3$.[33,34,38,39] Note that the analytical κ_{yy} values are used for

both calculated and measured $z_{xy}T$ because the direct measurement of κ_{yy} has never been done due to the difficulty to exclude the contaminated boundary effect. In the previous reports, although the higher $z_{xy}T$ than that of our SmCo$_5$/BST-based MCM has been predicted based on the analytical calculations, the measured large electrical resistances predominantly caused degradations in $z_{xy}T$ from the calculated ones. Thus, even if the analytical calculation suggests the higher $z_{xy}T$ values, the actual $z_{xy}T$ values can be lower due to the interfacial contributions ($z_{xy}T < 0.2$ when the analytically calculated κ_{yy} is used). In contrast, although the calculated $z_{xy}T$ value of our SmCo$_5$/based MCM is not the best, the extremely low interfacial resistances between the SmCo$_5$ and BST layers successfully suppress the performance degradation and realize the high $z_{xy}T$ value of 0.20 at room temperature. Thus, the introduction of SmCo$_5$ as the counterpart of BST not only provides the magnetic functionality but also contributes to the record-high transverse thermoelectric performance.

2.4 Giant transverse thermoelectric generation in the MCM-based module

In this section, we demonstrate giant transverse thermoelectric generation using SmCo$_5$/BST-based MCM. To achieve this, we developed a lateral thermopile module to enhance the thermoelectric voltage for a useful power supply to drive widely used electronic devices. Fig. 5a shows a schematic of the module structure, where the thin-sliced MCM elements are stacked with an opposite θ between the neighboring elements and intermediated by thin insulator layers. By electrically connecting the ends of neighboring MCMs, a long series circuit is formed so that $\mathbf{J}_c$ flows in a zigzag manner, as proposed by Norwood[1] and Kanno.[30] Importantly, the net magnetization of the thermopile module $\mathbf{M}_{net}$ is oriented along the ∇T direction by the vector sum of $\mathbf{M}$ in each MCM element. Thus, the MCM-based thermopile module operates as a permanent magnet. Fig. 5b shows the photograph of the constructed module, which is composed of 14 elements of magnetized SmCo$_5$/BST-based MCM (see the Experimental section for details). The fill factor of the MCM elements per heat transfer area exceeds 90% owing to the transverse geometry and very thin (approximately 0.05-mm-thick) insulator layers, ensuring a high thermoelectric output density and robustness against mechanical stress.[2,3] As shown in Fig. 5b, several ferromagnetic metal paper clips can be hung to the magnetized MCM-based module owing to its large $\mathbf{M}_{net}$. The internal resistance of the MCM-based module R_{module} was measured to be 34.8 mΩ by the four-terminal measurement, which deviates from the calculated R_{module} only by +11%. Thus, the contribution of the contact resistance between the MCM elements to the total resistance is also small. Fig. 5c shows a schematic of the measurement setup for transverse thermoelectric generation. The MCM-based module was sandwiched by the heater and heat bath to apply ∇T. The four-terminal voltage and power measurements were performed in the MCM-based module in the demagnetized state. The reason why the magnetic state (**M** and its stray field) of

This journal is © The Royal Society of Chemistry 2025

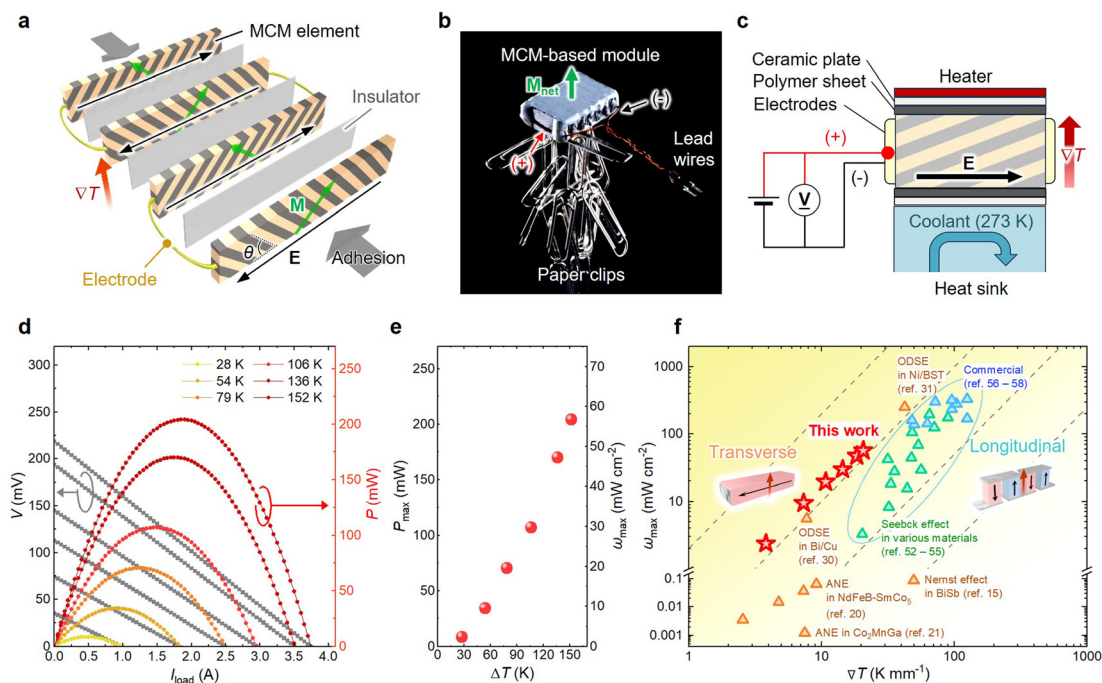*Energy Environ. Sci.*, 2025, **18**, 4068–4079 | **4073**

Fig. 5 Transverse thermoelectric generation by the MCM-based thermopile module. (a) Schematic of the architecture of the MCM-based thermopile module. The MCM elements are alternately stacked with opposite θ intermediated by thin insulator layers. By attaching electrodes to connect the ends of neighboring MCMs in a zigzag manner, a long series circuit is formed to sum up the transverse thermoelectric voltage. Net magnetization of the thermopile module M_{net} is oriented along the ∇T direction by the vector sum of M in each MCM element. (b) Photograph of the magnetized MCM-based module hanging many ferromagnetic metal paper clips owing to the large M_{net}. Lead wires are connected at the different sides $(+)/(-)$ of the thermopile circuit. (c) Schematic of the measurement setup for the transverse thermoelectric generation. (d) Load current I_{load} dependence of the thermoelectric voltage V and output power P at various values of the temperature difference ΔT. (e) ΔT dependence of the maximum output power P_{max} and maximum power density per heat transfer area ω_{max}. (f) ∇T dependence of ω_{max} for the MCM-based module used in this study (red stars), transverse (orange triangles) and longitudinal (green triangles) thermoelectric modules reported in the research papers, and commercial longitudinal thermoelectric modules (blue triangles). Gray dotted lines represent functions of $\omega_{max} = b\nabla T^2$ with b = 0.00025, 0.005, 0.1, and 2. A high $\omega_{max}/\nabla T^2$ is positioned to the left-upper corner as colored with yellow gradation on the background.

SmCo$_5$ does not contribute to the transverse thermoelectric performance is explained in Note S3 (ESI†).

Fig. 5d and e show the results of the transverse thermo-electric generation in the MCM-based module. In the load current I_{load} dependence of the thermoelectric voltage V (Fig. 5d), the open-circuit voltage V_{oc} is defined as the V value at I_{load} = 0 A and V linearly decreases with increasing I_{load} according to the internal resistance. P (= $I_{load}V$) shows a parabolic behavior against I_{load} and has a maximum value (P_{max}) when V is the half of V_{oc}. The V_{oc} and P_{max} values monotonically increased with increasing ΔT and reached 219 mV and 204 mW, respectively, at ΔT = 152 K, which are giant values for the transverse thermoelectric generation owing to the excellent $z_{xy}T$ with low interfacial electrical and thermal resistivities. Fig. 5e shows the ΔT dependence of P_{max} and the corresponding maximum power density ω_{max} per heat transfer area, which were almost parabolically increased with increasing ΔT as they are proportional to the square of V_{oc}, indicating almost no thermal deterioration of the thermoelectric properties at large ΔT. Consequently, ω_{max} reached 56.7 mW cm^{-2} at ΔT = 152 K owing to the transverse thermoelectric properties of MCM and the high fill factor of >90%. From the P_{max} value and the analytical transverse thermoelectric properties, we also

estimated the conversion efficiency for our MCM-based thermopile module at ΔT = 152 K to be 1.6–2.4% (Note S4 and Fig. S6, ESI†).

We compare the thermoelectric power generation performance of our MCM-based module with that of various transverse and longitudinal thermoelectric modules including commercial products. To fairly compare the intrinsic generation performance, we show the ∇T dependence of ω_{max} in Fig. 5f because the ω_{max} value is proportional to the square of ∇T and independent of the mechanism, geometry, and dimension of the thermoelectric modules. Gray dotted guide lines in Fig. 5f represent functions of $\omega_{max} = b\nabla T^2$ with b = 0.00025, 0.005, 0.1, and 2. Transverse thermoelectric modules utilizing the ordinary Nernst effect and ANE based on BiSb, Co$_2$MnGa, and Nd$_2$Fe$_{14}$B/SmCo$_5$ exhibit ω_{max} less than 0.1 mW cm^{-2} regardless of ∇T typically due to the low thermopower,[16,20,21] which has been the barrier towards applications of transverse thermoelectrics. Meanwhile, the transverse thermoelectric modules composed of Bi/Cu- and Ni/BST-based ATMLs reported higher ω_{max} of 5.5 and 250 mW cm^{-2} at ∇T = 7.8 and 42.5 K mm^{-1}, respectively.[30,31] However, the problem of the conventional ODSE-based module is the performance degradation due to the interfacial resistances. In this study,

by synthesizing high-performance MCM with extremely low interfacial resistances and constructing a high-density thermopile structure, we successfully demonstrated maximum ω_{max} of 56.7 mW cm^{-2} at ∇T of 20.7 K mm^{-1} (the red stars in Fig. 5f). Here, let us compare the normalized power density $\omega_{max}/\nabla T^2$ in the similar temperature range to exclude the contribution of ∇T. Then, our MCM-based module shows the record-high power generation performance of $\omega_{max}/\nabla T^2 = 0.17$ mW cm^{-2} (K mm^{-1})$^{-2}$ among all the transverse thermoelectric modules including Bi/Cu- and Ni/BST-based ATMLs (0.09 and 0.14 mW cm^{-2} (K mm^{-1})$^{-2}$, respectively). In Fig. 5f, we also show the ω_{max} values of the longitudinal thermoelectric modules utilizing the Seebeck effect, based on CoSb$_3$, Mg$_2$Si, Mg$_3$Sb$_2$, and Bi$_2$Te$_3$, including commercial products. The ω_{max} values are in the range of 15–497 mW cm^{-2} at ΔT of 120–200 K,[52–58] and the corresponding $\omega_{max}/\nabla T^2$ values are calculated to be less than 0.07 mW cm^{-2} (K mm^{-1})$^{-2}$. Surprisingly, the potential thermoelectric power density of our MCM-based module is larger than that of the commercial longitudinal thermoelectric modules. Thus, while having versatile transverse geometry and high mechanical durability,[1,7] our MCM-based module can generate the practical-level thermoelectric output power.

2.5 Efficient energy harvesting utilizing multifunctionality

In this section, we propose a new device concept where the multifunctionality of permanent magnet features and transverse thermoelectric conversion improves thermal energy harvesting performance even if the intrinsic material properties are unchanged. Fig. 6a shows a schematic of a cross-sectional view of the MCM-based module acting as a thermal energy harvester. The magnetic attractive force of the MCM-based module enables not only an easy installation onto a heat source made of a magnetic material but also an efficient heat input by eliminating the vacant space and reducing the contact thermal resistance between MCM and the heat source. In addition, the lateral thermopile geometry allows a surface area on the cool side to increase by changing the height of the neighboring MCM elements, enabling efficient heat release to the air atmosphere without attaching a heat bath; such a configuration is suitable for thermal energy harvesting. Hereafter, we refer to the device structure depicted in Fig. 6a as a built-in heat sink (BHS).

For this proof-of-concept demonstration, we prepared the MCM-based modules with and without BHS and compared their thermoelectric power generation performance without attaching a heat bath at the cold side. The three thermopile modules were constructed for the control experiment: (i) a demagnetized module without BHS, (ii) a magnetized module without BHS, and (iii) a magnetized module with BHS (see the Experimental section for details). The internal resistances of these modules are 20.4, 21.8, and 21.0 mΩ, respectively, which confirm almost the same volume and electrode contact conditions. The photograph in Fig. 6b shows the constructed modules (i) and (iii). Fig. 6c shows the experimental setup for the thermoelectric generation measurement under an air-cooled
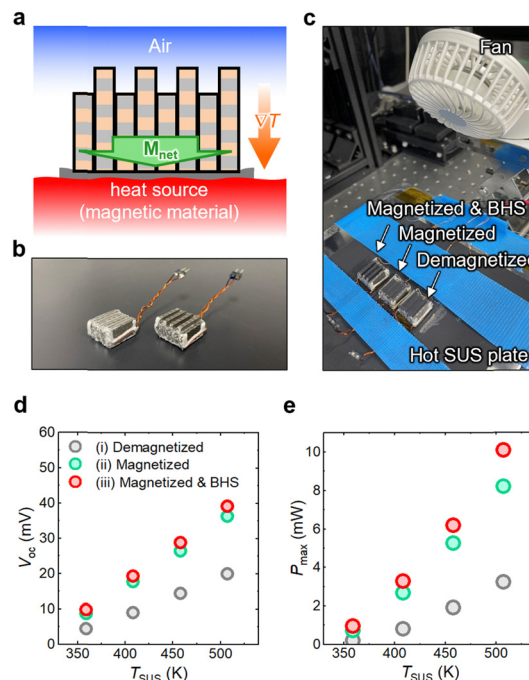

Fig. 6 Efficient energy harvesting utilizing multifunctionality. (a) Schematic of a cross-sectional view of the MCM-based thermopile module used as a thermal energy harvester. (b) Photograph of the MCM-based modules comprising 8 elements with (right) and without (left) BHS. (c) Photograph of the measurement setup for thermoelectric power generation by (i) a demagnetized module without BHS, (ii) a magnetized module without BHS, and (iii) a magnetized module with BHS. (d) and (e) the SUS plate temperature T_{SUS} dependence of the open-circuit voltage V_{oc} and P_{max} for (i)–(iii).

condition. A ferromagnetic steel use stainless (SUS) plate with dimensions of $150 \times 1 \times 150$ mm was coated with a black ink to observe the surface temperature of the SUS plate (T_{SUS}) using an infrared camera and heated using a ceramic hot plate. The three MCM-based modules (i)–(iii) were put on the SUS plate intermediated by 1-mm-thick insulating polymer sheets (MANION-SC, Sekisui Polymatech Co., Ltd). The copper wires connected to the modules were fixed by curing tapes (blue color parts in the photograph in Fig. 6c) so that the modules did not move during the measurement. The top surfaces were continuously cooled by an air flow using a personal fan to increase the heat transfer coefficient. After setting the temperature of the ceramic hot plate and waiting for 10 min, the four-terminal I_{load}–V measurements were performed.

Fig. 6d and e show V_{oc} and P_{max} as a function of T_{SUS} for the three MCM-based modules. All the modules show a linear increase of V_{oc} with the increase of T_{SUS}, which indicates that ∇T also linearly increases with T_{SUS} because of the almost constant S_{xy} with respect to the temperature (Fig. S4, ESI†). Importantly, the V_{oc} values obviously vary between the three MCM-based modules even though the intrinsic thermoelectric properties are almost the same. From the comparison between (i) and (ii), the magnetized module exhibits twice larger V_{oc} than the demagnetized module, suggesting the enhancement of ∇T by reducing the thermal contact resistance between the

This journal is © The Royal Society of Chemistry 2025

Energy Environ. Sci., 2025, **18**, 4068–4079 | **4075**

MCM-based module and the SUS plate. In addition, the comparison between (ii) and (iii) reveals that the introduction of the BHS leads to the enhancement of V_{oc} by $\sim 10\%$ owing to the efficient heat release to the air atmosphere. Thus, the installation of magnetic functionality and BHS successfully contribute to increase ∇T by the efficient heat transfer between the SUS plate, MCM-based module, and air. As a result of the increase of V_{oc}, P_{max} drastically increases (Fig. 6e). As demonstrated here, the multifunctionality of the magnetic attractive force and transverse thermoelectric conversion will bring about benefit for versatile thermoelectric applications through easy installation and efficient heat transfer.

3. Discussion

Herein, we discuss the possible future developments of MCMs in terms of the power generation performance. While the experimentally determined $z_{xy}T$ value of 0.20 for our MCM and the estimated conversion efficiency of 1.6–2.4% at $\Delta T = 152$ K for our MCM-based thermopile module are record-high among those of the transverse thermoelectric modules, the thermoelectric performance can be further improved through the following two approaches. One is the direct way to enhance ODSE by exploring permanent magnet materials with higher S and lower ρ than those of commercial SmCo$_5$-type magnets and optimizing interfacial microstructures with low electrical and thermal resistivities, as detailed in this work. Another approach involves hybridizing other mechanisms related to magnetism or spin. We have previously demonstrated the hybridization of the off-diagonal Peltier effect with the magneto-Peltier, ordinary Ettingshausen effects, and ANE in ATMLs,[40,59] where the calculated $z_{xy}T$ varies by 40% depending on an external magnetic field. In this study, we did not introduce such hybrid thermoelectric conversion to prioritize superior multifunctionality. However, it is possible to improve $z_{xy}T$ by hybridizing ANE and the Seebeck-effect-driven anomalous Hall effect in permanent magnets and/or the magneto-Seebeck effect in thermoelectric materials.[6,23,60] Thus, exploring magnetic materials with large anomalous Nernst and Hall effects is essential for further development of MCMs. Meanwhile, from the technological point of view, the magnetic attractive force enables an efficient heat input/output by reducing the contact thermal resistances between MCM and a heat source/bath made of a magnetic material.

4. Conclusions

We developed a novel functional material named MCM and demonstrated giant transverse thermoelectric generation in the MCM-based thermopile module. Our experiments showed that MCM consisting of alternately and obliquely stacked SmCo$_5$/BST multilayers exhibited an excellent $z_{xy}T$ of 0.20 at room temperature owing to the negligible negative effects of the interfacial resistances on the thermoelectric properties. Utilizing the high-performance MCM elements, we constructed a

lateral thermopile module and demonstrated a power generation of 204 mW at $\Delta T = 152$ K, which corresponds to the highest normalized power density of 0.17 mW cm^{-2} (K mm^{-1})$^{-2}$ among those of the transverse thermoelectric modules. MCM developed in this study paves the way toward new core technologies for energy harvesting and thermal management.

5. Experimental section

5.1 Sample preparation and characterization

SmCo$_5$/BST-based ATMLs were prepared as follows. Anisotropic SmCo$_5$-type magnet disks with a diameter of 20 mm and a thickness of 0.5 mm (YX24, Magfine Corporation) and BST alloy powder with 99.9% purity and a particle size of > 200 μm (Toshima Manufacturing Co., Ltd) were employed. The demagnetized SmCo$_5$ disks and BST powder were alternately stacked and bonded using SPS under a pressure of 30 MPa at 450 °C for 20–30 min, where the amount of BST powder per unit layer was approximately 1.05 g that was transformed to be 0.5-mm-thick after densification. Finally, the sintered stack was cut into a rectangular shape with θ of approximately 25°. To magnetize the sintered SmCo$_5$/BST multilayers, a pulse magnetic field of 8 T was applied in the direction perpendicular to the stacking plane. The plain BST slab was also prepared using the SPS method under the same sintering condition to measure the transport properties.

The temperature dependence of ρ and S of the SmCo$_5$ and BST slabs was measured using the Seebeck-coefficient/electric-resistance measurement system (ZEM-3, ADVANCE RIKO Inc.). The temperature dependence of κ was determined through thermal diffusivity measured using the laser flush method, specific heat measured using differential scanning calorimetry, and density measured using the Archimedes method. The magnetization M curve of SmCo$_5$ was measured via superconducting quantum interference device vibrating sample magnetometry using a Magnetic Property Measurement System (MPMS3, Quantum Design Inc.).

The elemental maps of the cross section of the SmCo$_5$/BST multilayer were obtained by SEM-EDX using a Cross-Beam 1540ESB (Carl Zeiss AG). To do this, the surface of the sample was mechanically polished in advance.

The interfacial electrical and thermal resistances of the SmCo$_5$/BST multilayer were characterized as described below. The SmCo$_5$/BST multilayer sample with $\theta = 0°$ and dimensions of $3.2 \times 11.2 \times 1.9$ mm was prepared. The position dependence of the four-terminal resistance was measured using the resistance distribution measuring instrument (Mottainai Energy Co., Ltd), where the contact probe was moved in 10-μm increments and alternating current with an amplitude of 100 mA was applied in the stacking direction. The LIT measurements were performed using Enhanced Lock-In Thermal Emission system (ELITE, DCG Systems G.K.) at room temperature and atmospheric pressure. The sample was fixed on a plastic plate with low thermal conductivity to reduce heat leakage due to thermal conduction. To enhance the infrared emissivity and

4076 | *Energy Environ. Sci.*, 2025, **18**, 4068–4079

This journal is © The Royal Society of Chemistry 2025

ensure uniform emission properties, the top surface of the sample was coated with an insulating black ink having an emissivity higher than 0.94 (JSC-3, JAPANSENSOR Corp.). The viewing areas of the thermal images in Fig. 3g and h and Fig. S1 (ESI†) are 1.54 × 1.74 mm and 7.68 × 3.84 mm, respectively.

The SmCo$_5$/BST multilayer sample with $\theta = 25°$ and dimensions of 12.4 × 8.3 × 1.1 mm was prepared for the direct measurements of S_{xy} and ρ_{xx}. The 8.3 × 1.1 mm surfaces were covered with Cerasolzer #297 (Kuroda Techno Co., Ltd) using the ultrasonic soldering technique to form electrodes for applying a uniform current. The copper wires were connected to the electrodes by Cerasolzer #186 (Kuroda Techno Co., Ltd) using the soldering iron. This sample was bridged between two anodized Al blocks, one of which is connected to chip heaters and the other to a heat bath to generate ∇T in the 8.3 mm direction. A central part of the 12.4 × 8.3 mm surface was covered with a black ink and the temperature distribution was measured with an infrared camera. The two Al–1%Si wires were directly connected to the 12.4 × 8.3 mm surface with a distance of 6.5 mm to measure the ac resistance and dc voltage. However the side surfaces were fully covered with a solder to have an alternating current uniformly input to MCM, and V and the ac resistance were measured between the point contacts inside MCM to exclude the boundary effect, which might cause the decrease in S_{xy} and ρ_{xx} compared with the analytical values.[26,28] The ac resistance was measured using a battery internal resistance tester (BT3562A, Hioki E.E. Corp.) applying an alternating current with an amplitude of 100 mA. The dc voltage under the application of ∇T was measured using a nanovoltmeter (2182A, Tektronix, Inc.).

5.2 Construction of the MCM-based thermopile module

The rectangular blocks of SmCo$_5$/BST-based ATML with $t = 0.5$ and $\theta = 25°$ were sliced into a rectangular shape with dimensions of 15.4 × 7.3 × 1.5 mm. To create electrodes to electrically connect the MCM elements in series, the 7.3 × 1.5 mm surfaces were firmly covered with Cerasolzer #297 (Kuroda Techno Co., Ltd) using the ultrasonic soldering technique. The 14 MCM elements were alternately stacked with the opposite θ and intermediated by 0.05-mm-thick insulating paper towels and heat-resistant glue (Duralco NM25, Cotronics Corp.). After curing for more than 4 h, the neighboring MCM elements were electrically connected to form a zigzag circuit by Cerasolzer #186 (Kuroda Techno Co., Ltd) using the soldering iron. At the ends of the thermopile circuit, enameled copper wires were connected using Cerasolzer #186 for power generation measurements. Finally, the heat transfer surfaces and the base of the copper wires were covered with the same heat-resistant glue to obtain smooth surfaces and fix the wires. The module shown in Fig. 5b was magnetized by a pulse magnetic field of 8 T along the direction of the heat current.

The three thermopile modules were constructed for the control experiment in Fig. 6: (i) a demagnetized module without BHS, (ii) a magnetized module without BHS, and (iii) a magnetized module with BHS. For (i) and (ii), 8 elements of SmCo$_5$/BST-based ATMLs with $t = 0.5$ and $\theta = 25°$ were prepared

with a rectangular shape of 12.2 × 7.3 × 1.5 mm. Meanwhile, for (iii), 4 elements with two different heights (8 elements in total) were alternately connected. To keep the same volume as those of (i) and (ii), the size of the smaller (larger) element was 12.2 × 6.3 × 1.5 mm (12.2 × 8.3 × 1.5 mm). To magnetize (ii) and (iii) after the construction, a pulse magnetic field of 8 T was applied along the direction of the heat current.

5.3 Transverse thermoelectric generation measurements

A custom-made sample holder was used to measure the transverse thermoelectric power generation. The MCM-based module was sandwiched between a heater plate and an aluminum heat sink. Ethylene glycol cooled at 273 K was circulated inside the heat sink during the measurements. To form uniform thermal contacts between the heater, module, and heat sink, 2-mm-thick AlN ceramic plates and 1-mm-thick insulating polymer sheets (MANION-SC, Sekisui Polymatech Co., Ltd) with a high thermal conductivity of approximately 25 W m^{-1} K^{-1} were inserted and screwed down, where the module was in direct contact with the polymer sheets (Fig. 5c). The side surface of the module was covered with insulating black ink to measure ΔT using an infrared camera. After the application and stabilization of ∇T for 10 min, the I_{load} dependence of V was measured three times and averaged. To characterize the internal resistance of the MCM-based module, the I_{load}–V curve was measured from −100 to +100 mA. To characterize the power generation performance, the I_{load}–V curve was measured from 0 to +6000 mA. The raw data of the I_{load}–V curves for the MCM-based module included the voltage drop due to the copper wires. Thus, the I_{load}–V curves only for two copper wires, whose ends were short-circuited using Cerasolzer #186, were subtracted from the raw data to evaluate the pure thermoelectric performance of the MCM-based module.

Author contributions

F. A. and K. U. conceived the idea, planned and supervised the study, designed the experiments, prepared the samples, developed an explanation of the results, and prepared the manuscript. F. A. and T. H. collected the data of the thermoelectric properties and LIT images. F. A. calculated the transverse thermoelectric properties. H. S. A. observed and analyzed the microstructure. F. A. and Y. I. analyzed the interfacial electrical resistance. A. A. and H. N. analyzed the interfacial thermal resistance. All the authors discussed the results and commented on the manuscript.

Data availability

The data supporting this article have been included as part of the ESI.†

Conflicts of interest

The authors declare no conflict of interest.

This journal is © The Royal Society of Chemistry 2025

Energy Environ. Sci., 2025, **18**, 4068–4079 | **4077**

Acknowledgements

References

1 M. H. Norwood, *J. Appl. Phys.*, 1963, **34**, 594–599.

2 G. Min and D. M. Rowe, *J. Power Sources*, 1992, **38**, 253–259.

3 D. M. Rowe, *Thermoelectrics Handbook: Macro to Nano*, CRC Press, New York, 2006.

4 K. Uchida and J. P. Heremans, *Joule*, 2022, **6**, 2240–2245.

5 A. Von Ettingshausen and W. Nernst, *Ann. Phys.*, 1886, **265**, 343–347.

6 A. W. Smith, *Phys. Rev.*, 1921, **17**, 23–37.

7 Y. Sakuraba, *Scr. Mater.*, 2016, **111**, 29–32.

8 M. Ikhlas, T. Tomita, T. Koretsune, M. T. Suzuki, D. Nishio-Hamane, R. Arita, Y. Otani and S. Nakatsuji, *Nat. Phys.*, 2017, **13**, 1085–1090.

9 A. Sakai, Y. P. Mizuta, A. A. Nugroho, R. Sihombing, T. Koretsune, M. T. Suzuki, N. Takemori, R. Ishii, D. Nishio-Hamane, R. Arita, P. Goswami and S. Nakatsuji, *Nat. Phys.*, 2018, **14**, 1119–1124.

10 H. Reichlova, R. Schlitz, S. Beckert, P. Swekis, A. Markou, Y. C. Chen, D. Kriegner, S. Fabretti, G. Hyeon Park, A. Niemann, S. Sudheendra, A. Thomas, K. Nielsch, C. Felser and S. T. B. Goennenwein, *Appl. Phys. Lett.*, 2018, **113**, 212405.

11 A. Miura, H. Sepehri-Amin, K. Masuda, H. Tsuchiura, Y. Miura, R. Iguchi, Y. Sakuraba, J. Shiomi, K. Hono and K. Uchida, *Appl. Phys. Lett.*, 2019, **115**, 222403.

12 S. N. Guin, P. Vir, Y. Zhang, N. Kumar, S. J. Watzman, C. Fu, E. Liu, K. Manna, W. Schnelle, J. Gooth, C. Shekhar, Y. Sun and C. Felser, *Adv. Mater.*, 2019, **31**, 1806622.

13 C. Wuttke, F. Caglieris, S. Sykora, F. Scaravaggi, A. U. B. Wolter, K. Manna, V. Süss, C. Shekhar, C. Felser, B. Büchner and C. Hess, *Phys. Rev. B*, 2019, **100**, 085111.

14 A. Sakai, S. Minami, T. Koretsune, T. Chen, T. Higo, Y. Wang, T. Nomoto, M. Hirayama, S. Miwa, D. Nishio-Hamane, F. Ishii, R. Arita and S. Nakatsuji, *Nature*, 2020, **581**, 53–57.

15 A. Miura, K. Masuda, T. Hirai, R. Iguchi, T. Seki, Y. Miura, H. Tsuchiura, K. Takanashi and K. Uchida, *Appl. Phys. Lett.*, 2020, **117**, 082408.

16 M. Murata, K. Nagase, K. Aoyama, A. Yamamoto and Y. Sakuraba, *iScience*, 2021, **24**, 101967.

17 T. Asaba, V. Ivanov, S. M. Thomas, S. Y. Savrasov, J. D. Thompson, E. D. Bauer and F. Ronning, *Sci. Adv.*, 2021, **7**, eabf1467.

18 B. He, C. Şahin, S. R. Boona, B. C. Sales, Y. Pan, C. Felser, M. E. Flatté and J. P. Heremans, *Joule*, 2021, **5**, 3057–3067.

19 Y. Pan, C. Le, B. He, S. J. Watzman, M. Yao, J. Gooth, J. P. Heremans, Y. Sun and C. Felser, *Nat. Mater.*, 2022, **21**, 203–209.

20 F. Ando, T. Hirai and K. Uchida, *APL Energy*, 2024, **2**, 016103.

21 M. Chen, J. Wang, K. Liu, W. Fan, Y. Sun, C. Felser, T. Zhu and C. Fu, *Adv. Energy Mater.*, 2024, 2400411.

22 K. Uchida, S. Takahashi, K. Harii, J. Ieda, W. Koshibae, K. Ando, S. Maekawa and E. Saitoh, *Nature*, 2008, **455**, 778–781.

23 W. Zhou, K. Yamamoto, A. Miura, R. Iguchi, Y. Miura, K. Uchida and Y. Sakuraba, *Nat. Mater.*, 2021, **20**, 463–467.

24 C. L. Chang, A. Kleinhammes, W. G. Moulton and L. R. Testardi, *Phys. Rev. B:Condens. Matter Mater. Phys.*, 1990, **41**, 11564–11567.

25 T. Zahner, R. Förg and H. Lengfellner, *Appl. Phys. Lett.*, 1998, **73**, 1364–1366.

26 T. Kanno, S. Yotsuhashi, A. Sakai, K. Takahashi and H. Adachi, *Appl. Phys. Lett.*, 2009, **94**, 061917.

27 H. J. Goldsmid, *J. Electron. Mater.*, 2011, **40**, 1254–1259.

28 T. Kanno, A. Sakai, K. Takahashi, A. Omote, H. Adachi and Y. Yamada, *Appl. Phys. Lett.*, 2012, **101**, 011906.

29 C. Zhou, S. Birner, Y. Tang, K. Heinselman and M. Grayson, *Phys. Rev. Lett.*, 2013, **110**, 227701.

30 T. Kanno, K. Takahashi, A. Sakai, H. Tamaki, H. Kusada and Y. Yamada, *J. Electron. Mater.*, 2014, **43**, 2072–2080.

31 A. Sakai, T. Kanno, K. Takahashi, H. Tamaki, H. Kusada, Y. Yamada and H. Abe, *Sci. Rep.*, 2014, **4**, 6089.

32 Y. Tang, B. Cui, C. Zhou and M. Grayson, *J. Electron. Mater.*, 2015, **44**, 2095–2104.

33 X. Mu, H. Zhou, W. Zhao, D. He, W. Zhu, X. Nie, Z. Sun and Q. Zhang, *J. Power Sources*, 2019, **430**, 193–200.

34 W. Zhu, X. Guo, X. Sang, P. Wei, X. Nie, W. Zhao and Q. Zhang, *J. Power Sources*, 2021, **512**, 230471.

35 M. R. Scudder, B. He, Y. Wang, A. Rai, D. G. Cahill, W. Windl, J. P. Heremans and J. E. Goldberger, *Energy Environ. Sci.*, 2021, **14**, 4009–4017.

36 M. R. Scudder, K. G. Koster, J. P. Heremans and J. E. Goldberger, *Appl. Phys. Rev.*, 2022, **9**, 021420.

37 H. Zhou, H. Liu, G. Qian, H. Yu, X. Gong, X. Li and J. Zheng, *Micromachines*, 2022, **13**, 233.

38 K. Yue, W. Zhu, Q. He, X. Nie, X. Qi, C. Sun, W. Zhao and Q. Zhang, *ACS Appl. Mater. Interfaces*, 2022, **14**, 39053–39061.

39 W. Zhu, H. Zhou, P. Wei, C. Sun, D. He, X. Nie, X. Sang, W. Zhao and Q. Zhang, *J. Eur. Ceram. Soc.*, 2022, **42**, 3913–3919.

40 K. Uchida, T. Hirai, F. Ando and H. Sepehri-Amin, *Adv. Energy Mater.*, 2024, **14**, 2302375.

41 K. Kumar, *J. Appl. Phys.*, 1988, **63**, 13–57.

42 R. He, G. Schierning and K. Nielsch, *Adv. Mater. Technol.*, 2018, **3**, 1700256.

43 J. Chu, J. Huang, R. Liu, J. Liao, X. Xia, Q. Zhang, C. Wang, M. Gu, S. Bai, X. Shi and L. Chen, *Nat. Commun.*, 2020, **11**, 2723.

44 L. Xie, L. Yin, Y. Yu, G. Peng, S. Song, P. Ying, S. Cai, Y. Sun, W. Shi, H. Wu, N. Qu, F. Guo, W. Cai, H. Wu, Q. Zhang,

4078 | *Energy Environ. Sci.*, 2025, **18**, 4068–4079

This journal is © The Royal Society of Chemistry 2025

K. Nielsch, Z. Ren, Z. Liu and J. Sui, *Science*, 2023, **382**, 921–928.

45 R. P. Gupta, O. D. Iyore, K. Xiong, J. B. White, K. Cho, H. N. Alshareef and B. E. Gnade, *Electrochem. Solid-State Lett.*, 2009, **12**, 395–397.

46 X. Wang, Z. Zhou, P. Zhang, S. Zhang, Y. Ma, W. Yang, H. Wang, B. Li, L. Meng, H. Jiang, S. Cui, P. Zhai, J. Xiao, W. Liu, X. Zou, L. Bao and Y. Gong, *Chem. Mater.*, 2020, **32**, 2321–2329.

47 W. Bin Wu, Y. Q. Chen, Q. L. Xiao and J. Y. Ge, *J. Alloys Compd.*, 2024, **983**, 173884.

48 O. Breitenstein, W. Warta and M. Langenkamp, *Lock-in Thermography: Basics and Use for Evaluating Electronic Devices and Materials*, Springer, Berlin, Heidelberg, 2nd edn, 2010.

49 T. Ishizaki, T. Igami and H. Nagano, *Rev. Sci. Instrum.*, 2020, **91**, 064901.

50 A. Alasli, A. Miura, R. Iguchi, H. Nagano and K. Uchida, *Sci. Technol. Adv. Mater. Meth.*, 2021, **1**, 162–168.

51 A. Alasli, T. Hirai, H. Nagano and K. Uchida, *Appl. Phys. Lett.*, 2022, **121**, 154104.

52 J. R. Salvador, J. Y. Cho, Z. Ye, J. E. Moczygemba, A. J. Thompson, J. W. Sharp, J. D. Koenig, R. Maloney, T. Thompson, J. Sakamoto, H. Wang and A. A. Wereszczak, *Phys. Chem. Chem. Phys.*, 2014, **16**, 12510–12520.

53 G. Skomedal, L. Holmgren, H. Middleton, I. S. Eremin, G. N. Isachenko, M. Jaegle, K. Tarantik, N. Vlachos, M. Manoli, T. Kyratsi, D. Berthebaud, N. Y. Dao Truong and F. Gascoin, *Energy Convers. Manage.*, 2016, **110**, 13–21.

54 R. Deng, X. Su, S. Hao, Z. Zheng, M. Zhang, H. Xie, W. Liu, Y. Yan, C. Wolverton, C. Uher, M. G. Kanatzidis and X. Tang, *Energy Environ. Sci.*, 2018, **11**, 1520–1535.

55 Z. Liu, N. Sato, W. Gao, K. Yubuta, N. Kawamoto, M. Mitome, K. Kurashima, Y. Owada, K. Nagase, C. H. Lee, J. Yi, K. Tsuchiya and T. Mori, *Joule*, 2021, **5**, 1196–1208.

56 KELK Ltd., Products information on thermo generation module, **https://www.kelk.co.jp/english/generation/index.html**.

57 Coherent Corp., Thermoelectric Generator (TEG) Modules, **https://ii-vi.com/product/thermoelectric-generator-teg-modules/**.

58 Ferrotec Materials Technologies Corp., Power Generation Thermoelectric Modules, **https://ft-mt.co.jp/en/product/electronic_device/thermo/power_generation/**, (accessed 15 January 2024).

59 T. Hirai, F. Ando, H. Sepehri-Amin and K. Uchida, *Nat. Commun.*, 2024, **15**, 9643.

60 T. C. Harman, J. M. Honig, S. Fischler and A. E. Paladino, *Solid-State Electron.*, 1964, **7**, 505–508.